

Enhanced Carrier Collection in Cd/In-Based Dual Buffers in Kesterite Thin-Film Solar Cells from Nanoparticle Inks

Stephen Campbell, Guillaume Zoppi, Leon Bowen, Pietro Maiello, Vincent Barrioz, Neil S. Beattie, and Yongtao Qu*



Cite This: *ACS Appl. Energy Mater.* 2023, 6, 10883–10896



Read Online

ACCESS |

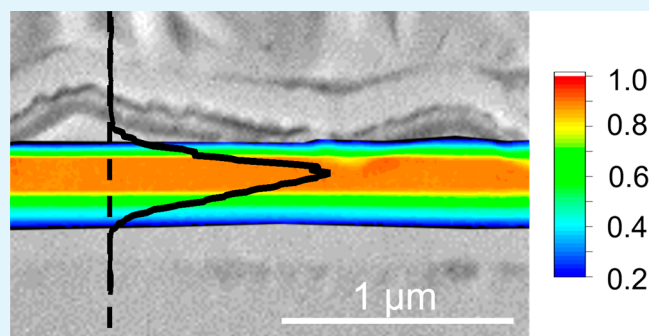
Metrics & More

Article Recommendations

Supporting Information

ABSTRACT: Increasing the power conversion efficiency (PCE) of kesterite $\text{Cu}_2\text{ZnSn}(\text{S},\text{Se})_4$ (CZTSSe) solar cells has remained challenging over the past decade, in part due to open-circuit voltage (V_{OC})-limiting defect states at the absorber/buffer interface. Previously, we found that substituting the conventional CdS buffer layer with In_2S_3 in CZTSSe devices fabricated from nanoparticle inks produced an increase in the apparent doping density of the CZTSSe film and a higher built-in voltage arising from a more favorable energy-band alignment at the absorber/buffer interface. However, any associated gain in V_{OC} was negated by the introduction of photoactive defects at the interface. This present study incorporates a hybrid Cd/In dual buffer in CZTSSe devices that demonstrate an average relative increase of 11.5% in PCE compared to CZTSSe devices with a standard CdS buffer. Current density–voltage analysis using a double-diode model revealed the presence of (i) a large recombination current in the quasi-neutral region (QNR) of the CZTSSe absorber in the standard CdS-based device, (ii) a large recombination current in the space-charge region (SCR) of the hybrid buffer CZTSSe– In_2S_3 –CdS device, and (iii) reduced recombination currents in both the QNR and SCR of the CZTSSe–CdS– In_2S_3 device. This accounts for a notable 9.0% average increase in the short-circuit current density (J_{SC}) observed in CZTSSe–CdS– In_2S_3 in comparison to the CdS-only CZTSSe solar cells. Energy-dispersive X-ray, secondary-ion mass spectroscopy, and grazing-incidence X-ray diffraction compositional analysis of the CZTSSe layer in the three types of kesterite solar cells suggest that there is diffusion of elemental In and Cd into the absorbers with a hybrid buffer. Enhanced Cd diffusion concomitant with a double postdeposition heat treatment of the hybrid buffer layers in the CZTSSe–CdS– In_2S_3 device increases carrier collection and extraction and boosts J_{SC} . This is evidenced by electron-beam-induced current measurements, where higher current generation and collection near to the p–n junction is observed, accounting for the increase in J_{SC} in this device. It is expected that optimization of the heat treatment of the hybrid buffer layers will lead to further improvements in the device performance.

KEYWORDS: kesterite, CZTSSe, nanoparticle inks, In_2S_3 –CdS buffer, EBIC



INTRODUCTION

Among all renewable energy sources (wind, water, solar, etc.), photovoltaic (PV) technology is the most promising way to harvest ambient light energy silently and unobtrusively into electricity, committing to the net-zero greenhouse emission strategy.¹ Closely related to the prominent thin-film technology copper–indium–gallium selenide but with increased Earth abundance of the constituent elements, kesterite emerged as one of the most promising PV absorber materials because of its low cost and excellent and stable optoelectronic properties.^{2,3} To date, $\text{Cu}_2\text{ZnSn}(\text{S},\text{Se})_4$ (CZTSSe) thin-film solar cells (TFSCs) demonstrated promising power conversion efficiencies (PCEs) of 13.8% (certified) and 14.9% (reported) at the laboratory scale,^{4–6} while the theoretically predicted efficiency for kesterites is over 32%, which gives large motivation and window to further enhance the device performance.

Importantly, kesterite solar cells made from nanoparticle inks have the potential to provide disruptively high specific power solar modules on flexible substrates that are ideal for integration to “self-powered” distributed Internet of Things (IoT) applications.^{7–11}

While TFSCs fabricated from a kesterite absorber provide an Earth-abundant and stable energy-harvesting solution, their commercialization has been historically restricted, in part due to their V_{OC} -limiting defect states at both the absorber bulk

Received: June 30, 2023

Revised: October 5, 2023

Accepted: October 5, 2023

Published: October 27, 2023



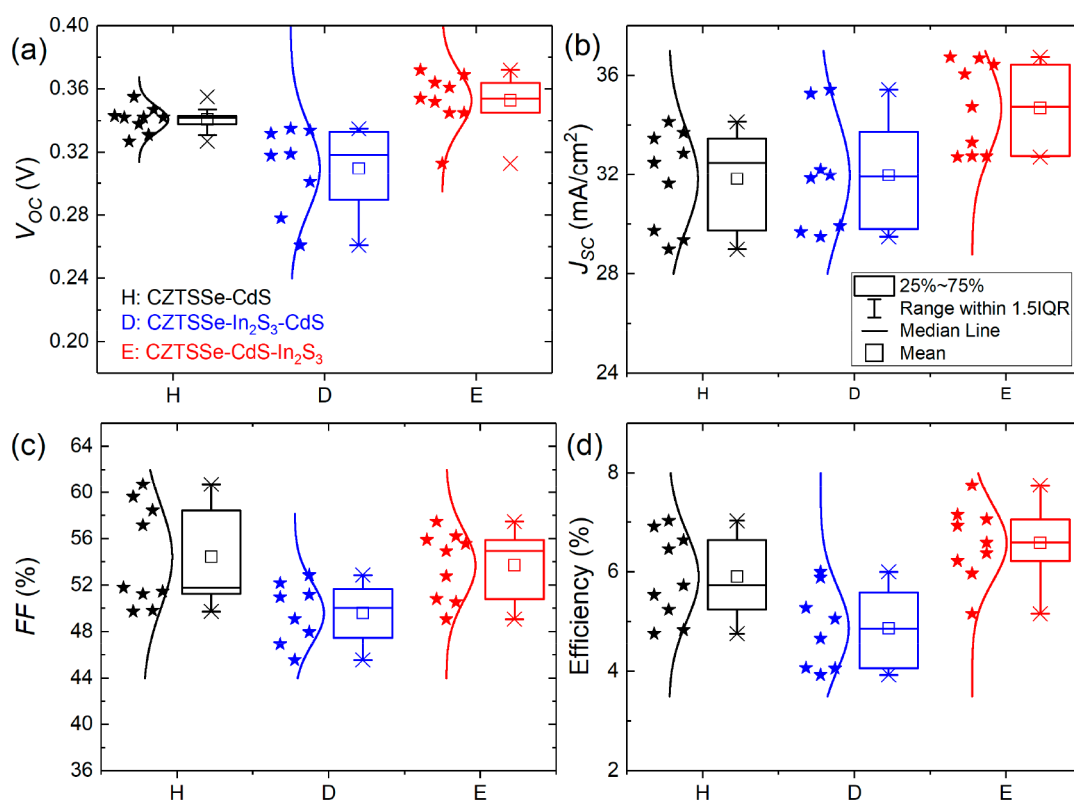


Figure 1. Box plots of the distribution of (a) V_{OC} , (b) J_{SC} , (c) FF, and (d) efficiency of all nine cells for each device structure. The \square symbol is the average value, and the \times symbol represents minimum and maximum values. The three horizontal lines of each box represent 25%, 50%, and 75% of the data distribution. The whisker range is determined by the standard deviation of the data.

and absorber/buffer interface.^{12,13} It was found that substituting the conventional CdS buffer layer with In_2S_3 in kesterite devices produced an increase in the apparent doping density of the CZTSSe film and a higher built-in voltage arising from a more favorable energy-band alignment at the absorber/buffer interface.^{14–16} However, any associated gain in V_{OC} was negated by the introduction of photoactive defects at the interface, as reported in our previous work.¹⁷ It is believed that elemental doping due to interdiffusion at absorber/buffer heterojunctions plays an important role in passivating interface defects and determining the kesterite solar cells' performance.^{18,19}

In this study, therefore, a CdS/ In_2S_3 hybrid buffer structure was explored in CZTSSe devices to understand how the buffer structure will influence the elemental diffusion at the heterojunction and determine the device performance. Spectral response measurements of hybrid buffer devices confirmed the presence of photoactive interface defects when the In_2S_3 buffer is adjacent to the CZTSSe absorber. Current density–voltage analysis using a double-diode model revealed the presence of (i) a large recombination current in the quasi-neutral region (QNR) of the CZTSSe absorber in the standard CdS-based device, (ii) a large recombination current in the space-charge region (SCR) of the hybrid buffer CZTSSe– In_2S_3 –CdS device, and (iii) reduced recombination currents in both the QNR and SCR of the CZTSSe–CdS– In_2S_3 device. Further measurement including energy-dispersive X-ray (EDX), secondary-ion mass spectroscopy (SIMS), and grazing-incidence X-ray diffraction (GIXRD) compositional analysis of the CZTSSe layer in the three types of kesterite solar cells suggests that there is diffusion of elemental In into the

absorbers with a hybrid buffer. We found that a middle CdS layer between the CZTSSe absorber and top In_2S_3 buffer is essential to provide a proper doping density of the SCR region of CZTSSe without adversely affecting the overall device performance. Hereafter, devices with structures CZTSSe–CdS, CZTSSe– In_2S_3 –CdS, and CZTSSe–CdS– In_2S_3 will be referred to as devices H, D, and E, respectively.

RESULTS AND DISCUSSION

Device Characteristics. Figure 1 shows the distribution of device parameters in the CZTSSe solar cells with different buffers, with Table 1 showing the average parameter values for

Table 1. Average Device Parameters for the CZTSSe Solar Cells, with the Best-Performing Device Values in Parentheses

device type	V_{OC} (mV)	J_{SC} (mA/cm^2)	FF (%)	efficiency (%)
H: CZTSSe–CdS	341 (355)	31.8 (34.1)	54.5 (60.7)	5.90 (7.03)
D: CZTSSe– In_2S_3 –CdS	310 (335)	32.0 (35.4)	49.6 (52.9)	4.87 (6.00)
E: CZTSSe–CdS– In_2S_3	353 (372)	34.7 (36.7)	53.7 (57.5)	6.58 (7.75)

a set of nine solar cells (champion device values in parentheses). Evident is the increase in the open-circuit voltage (V_{OC}), short-circuit current density (J_{SC}), and PCE (η) of device E compared to the other devices. Device D generally performed worse than the other two devices. Both device sets with a dual buffer exhibit a fill factor (FF) lower than that of the standard devices with a single CdS buffer. The decrease in

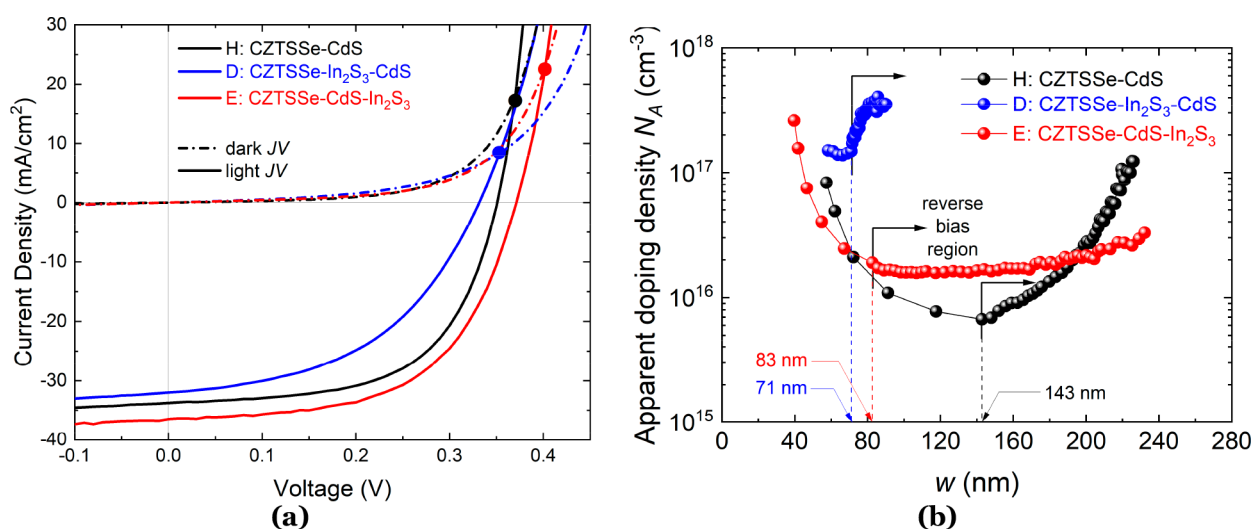


Figure 2. (a) Light (solid lines) and dark (dash-dotted lines) J - V curves for all champion device types. Solid circles mark the crossover points between light and dark J - V plots. (b) C - V depth profiles with indicated w_{SCR} values at zero bias.

FF for devices with a dual buffer layer can be directly related to an increase in the series resistance (R_S) for those devices. The typical R_S value for the dual buffer cells studied is $\sim 1.9 \Omega \text{ cm}^2$ compared to $\sim 1.0 \Omega \text{ cm}^2$ for the reference CdS-buffered cells, while the shunt resistance (R_{SH}) was similar in all device types ($\sim 140 \Omega \text{ cm}^2$). Higher R_S in the dual buffer devices can be attributed to an increase in the combined thickness of the CdS/In₂S₃ layers (see the [Electron Microscopy and Composition](#) section).²⁰ Most notable is the average increase in J_{SC} of type E solar cells (34.7 mA/cm^2) compared to those of types H (31.8 mA/cm^2) and D (32.0 mA/cm^2), with champion device E achieving a J_{SC} of 36.7 mA/cm^2 . Subsequently, this solar cell achieved a PCE of 7.75%. The J - V curves of champion solar cells for all device types measured in the dark and under 1-sun illumination are plotted in [Figure 2a](#).

The dark and illuminated J - V curves exhibit crossover behavior, which is indicative of an electrical barrier either in the buffer/absorber interface or at the absorber/Mo metal contact due to a thick interfacial layer of MoSe₂.^{21–23} Because all devices fabricated for this study were made from the same batch of CZTS nanoparticle inks and subjected to the same selenization conditions, it is unlikely that a thick MoSe₂ layer is the cause of the low crossover point. Our previous studies have shown that CZTSSe devices fabricated from CZTS nanoparticle inks typically have a low hole barrier of $\sim 40 \text{ meV}$ at the back-contact, suggesting that the back-contact is not the predominant factor influencing carrier extraction.^{19,24} This suggests that a current-blocking barrier exists at the buffer/absorber interface in all types of devices, with a higher barrier present when In₂S₃ is deposited directly on top of the CZTSSe absorber (indicated by the lower J - V crossover point in device D). The dark J - V curves in [Figure 2a](#) were fitted using the double-diode model for an n^+ - p device ([Figure S1](#)), described by

$$J = J_{01} \left[\exp\left(\frac{q(V + JR_S)}{kT}\right) - 1 \right] - J_{02} \left[\exp\left(\frac{q(V + JR_S)}{2kT}\right) - 1 \right] - \frac{V + JR_S}{R_{SH}} \quad (1)$$

where k is the Boltzmann constant, T is the temperature, R_S is the series resistance, R_{SH} is the shunt resistance, and J_{01} and J_{02} are the reverse saturation currents relating to the recombination currents in the QNR and SCR of the solar cell, respectively ([Table 2](#)). Practical fitting of the illuminated J -

Table 2. Recombination Current Values (J_{01} and J_{02}) of the Best-Performing Cells for Each Device Type Determined by Double-Diode Analysis (According to [Equation 1](#)) with the Apparent Doping Density (N_A) and SCR Width (w_{SCR}) of the Corresponding Devices

device type	J_{01} QNR (mA/cm ²)	J_{02} SCR (mA/cm ²)	w_{SCR} (nm)	N_A (cm ⁻³)
H: CZTSSe-CdS	2.6×10^{-4}	4.6×10^{-2}	143	8.9×10^{15}
D: CZTSSe-In ₂ S ₃ -CdS	1.6×10^{-6}	6.4×10^{-1}	71	1.7×10^{17}
E: CZTSSe-CdS-In ₂ S ₃	7.2×10^{-5}	6.9×10^{-3}	83	1.6×10^{16}

V curves is difficult because small fluctuations in the light intensity overwhelm the effects of the second diode, which relates to the SCR. It is apparent that device E has a lower recombination current in the SCR ($J_{02} = 6.9 \times 10^{-3} \text{ mA/cm}^2$) compared to the other device types (H, $J_{02} = 4.6 \times 10^{-2} \text{ mA/cm}^2$; D, $J_{02} = 6.4 \times 10^{-1} \text{ mA/cm}^2$), which is concomitant with higher J_{SC} observed in type E devices. Conversely, device D shows a lower recombination current in the bulk of the CZTSSe absorber, where $J_{01} = 1.6 \times 10^{-6} \text{ mA/cm}^2$ in contrast to J_{01} values of 2.6×10^{-4} and $7.3 \times 10^{-5} \text{ mA/cm}^2$ for devices H and E, respectively ([Table 2](#)). Explanations for this behavior will be explored in the [Results and Discussion](#) section. The performance of kesterite solar cells can be limited by heterojunction interface defects and deep-level defects in the SCR.^{25–27}

Capacitance-voltage (C - V) profiling measurements were performed to determine the apparent doping density (N_A), SCR width (w_{SCR}), and built-in potential (V_{BI}) of all device types. When the bias voltage is set to $V = 0$, N_A and V_{BI} can be determined from Mott-Schottky analysis of the C - V data, which is expressed by $N_A = -2(dC^{-2}/dV)/q\epsilon_0\epsilon_r$, where C is the capacitance/cell area, ϵ_0 is the permittivity of free space, and ϵ_r is the dielectric constant of CZTSSe ([Figure S2](#)). As

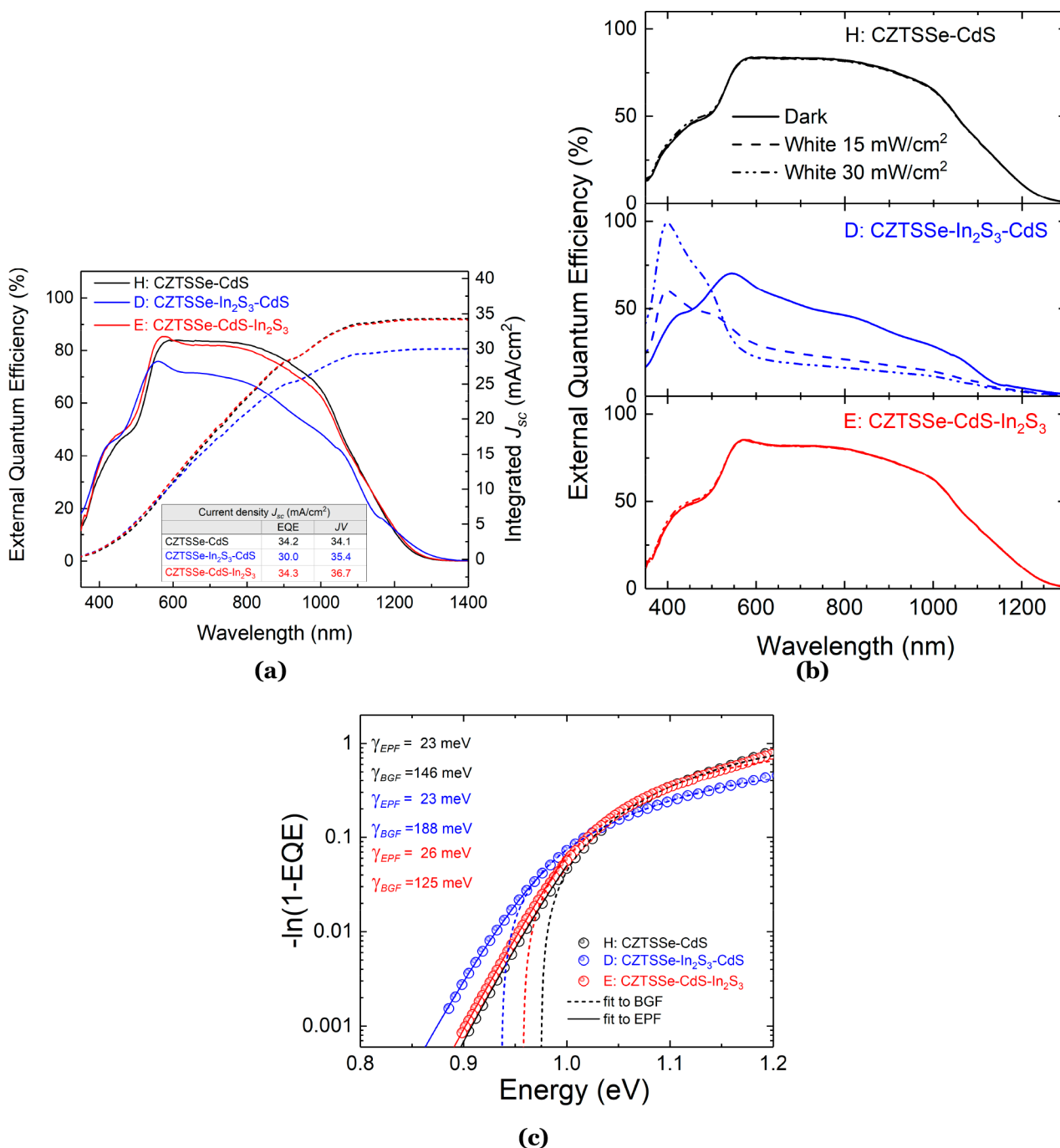


Figure 3. (a) EQE spectra with integrated J_{sc} of the best cells with an area of 0.16 cm². (b) EQE with white-light bias (at 15 and 30 mW/cm²) and without light bias (dark) for different device types. (c) Fitting of the absorption coefficient α [$\alpha \ln(1 - EQE)$] below the band gap of each device to estimate the magnitude of electrostatic potential fluctuations (γ_{EPF}) and band-gap fluctuations (γ_{BGF}).

such, built-in voltages of 0.182, 0.841, and 0.126 V were determined for devices H, D, and E, respectively. The relatively high V_{BI} value observed in device D is likely due to a positive “spike-like” conduction band offset at the CZTSSe/In₂S₃ interface, which was demonstrated in our previous study of CZTSSe solar cells with a In₂S₃ buffer.¹⁷

Devices with a large V_{BI} should have a correspondingly high V_{OC} , which is not the case for devices with the structure CZTSSe-In₂S₃-CdS and could be related to increased levels of defects at the buffer/absorber interface. Additionally, N_A values of 8.4×10^{15} , 1.8×10^{17} , and 1.7×10^{16} cm⁻³ were determined for devices H, D, and E, respectively (Table 2).

The notable increase in the doping density for device D has previously been observed in kesterite solar cells, which employ In₂S₃ as a buffer layer and was ascribed to significant In diffusion into the absorber as a result of device processing conditions.^{14,15,18} Elemental diffusion into the CZTSSe absorber will be addressed in detail in the Results and Discussion section. Figure 2b shows the apparent doping density profile at a distance w from the p-n junction width. Devices H and D show a “U”-shaped depth-dependent doping profile often seen in thin-film chalcopyrite and kesterite solar cells, with a minimum doping concentration typically in the range of a few 10^{15} cm⁻³ for moderate applied voltage bias with

significantly higher doping density at high forward and reverse bias.^{17,28–31} An increase in the apparent doping density toward increasing forward bias has been attributed to minority carrier injection and parasitic resistances and the increase with higher reverse bias related to the presence of deep defects.³² Werner et al. have suggested that the SCR capacitance in TFSCs containing Cd- or Zn-incorporated buffers follows the model of a linearly graded junction and is a result of elemental intermixing at the buffer/absorber interface, which alters the apparent doping concentration.²⁸ However, device E shows an extended flat region in the depth-dependent doping profile, suggesting a more uniform doping concentration that extends from the region near the buffer/absorber interface into the bulk of the CZTSSe absorber. The SCR width (w_{SCR}) is calculated to be 143, 71, and 83 nm for devices H, D, and E, respectively. Both device types with a dual buffer exhibit a significant narrowing of the SCR compared to the standard device. This can be directly attributed to the higher doping density observed in the devices with a dual buffer because the SCR width ratio of n-to-p-type semiconductors in a p–n junction is equal to the ratio of apparent acceptor-to-donor density, i.e., $w_{\text{SCR,p}}/w_{\text{SCR,n}}$ where $w_{\text{SCR,p}}$ and $w_{\text{SCR,n}}$ are the SCR widths in p- and n-type semiconductors, respectively, and N_{D} and N_{A} are the apparent donor and acceptor densities, respectively (Table 2). From Table 2, it appears that the apparent doping density of the CZTSSe absorbers in the studied devices is linked to the recombination current in the SCR of their respective devices. To gain deeper insight into the carrier collection efficiency, external quantum efficiency (EQE) measurements were performed on all device types, with the results shown in Figure 3a. The spectra showed similar responses, whereby a steep rise in current collection is observed in the ultraviolet-blue region (<450 nm), followed by steady collection in the region of 600–850 nm and a gradual decrease at wavelengths of >850 nm. Both types of dual buffer devices showed increased current extraction at wavelengths of >550 nm due to the presence of a slightly thinner CdS layer and higher transmittance in the In_2S_3 layer.¹⁷ The most notable difference in the EQE spectra is the drop in response of device D over wavelengths of >550 nm, which could be linked to a poor minority carrier diffusion length coupled with a narrow w_{SCR} . Because effective charge separation occurs in the depletion region in the absorber material of a solar cell, such a small w_{SCR} due to a high hole concentration in CZTSSe adversely affects the carrier collection. The overall lower collection efficiency in this device would also suggest a higher barrier to minority carrier (electron) transport, which is in agreement with the lower J – V crossover for this device seen in Figure 2a. A similar behavior has been observed in other kesterite solar cells that employ a In_2S_3 buffer.^{14,33,34} By definition, EQE represents the ratio between the numbers of generated charge carriers to the number of incident photons; therefore, J_{SC} can be estimated by integrating the EQE over the entire spectrum. The comparative results between J_{SC} extracted from J – V and EQE analysis are shown as a table inset in Figure 3a. It is evident that devices with a dual buffer layer have lower J_{SC} when calculated from EQE spectra. Similar results have been observed previously and were attributed to the photoactive nature of the In_2S_3 layer and the CZTSSe/ In_2S_3 interface, which can influence defects and interface recombination.^{14,35} The band gaps E_{G} of the CZTSSe absorbers in each type of device were determined from EQE measurements (Figure S3),

yielding values of 1.143, 1.187, and 1.143 eV for devices H, D, and E, respectively. Xiao et al. studied the effects of In doping on CZTS and CZTSe solar cells and found that an increasing In/Sn ratio (or In content) caused a monotonic increase in the absorber band gap.³⁶ Therefore, In diffusion from the In_2S_3 buffer into the CZTSSe film due to In_2S_3 /CdS film deposition/heat treatment could account for the increased band gap seen in device D.

Additionally, light-biased EQE measurements were done to study the effects of white-light illumination (at 15 and 30 mW/cm²) on absorption in the CZTSSe films of each device type (Figure 3b). There is little discernible difference between the unbiased and biased EQE spectra for devices H and E, while the light-biased EQE response of device D is higher in the blue part of the spectrum (wavelengths of <500 nm) and significantly lower over the remaining spectrum (wavelengths of >500 nm). This phenomenon has also been previously observed in kesterite CZTS solar cells with a CdS and/or In_2S_3 buffer layer,^{14,35} which was ascribed to saturated and unsaturated photoactive defects in the CdS and In_2S_3 layers, respectively. Under white-light illumination, these photoactive defects shrink the width of the SCR by the optical injection of red photons, and the effect is more pronounced in the device with an In_2S_3 buffer directly on top of the CZTSSe absorber, due to the unsaturated nature of the defects present in this film.

In a nonideal semiconductor with high defect densities, band tail states allow the absorption of photons with sub-band-gap energies. The sub-band-gap absorption in CZTSSe can be modeled in several ways: (i) Urbach tail states; (ii) band-gap fluctuations (BGF); (iii) electrostatic potential fluctuations (EPF).^{17,37} It is evident from the EQE spectra in Figure 3a that there is significant absorption of sub-band-gap photons in all device types, and further analysis is required to determine the cause. It is possible to quantify the origins of band tailing utilizing the relationship between the absorption coefficient (α) of a semiconductor and EQE. EQE is proportional to α such that $\alpha \propto -\ln[1 - \text{EQE}(h\nu)]$ ³⁸ and depends on the density of states in the fluctuating potentials of the conduction and valence energy bands. Regarding band-gap fluctuations (γ_{BGF}), the model assumes a Gaussian distribution of band-gap energies centered at $E_{\text{G,mean}}$ and characterized by a standard deviation σ where $\sigma \equiv \gamma_{\text{BGF}}$.^{39,40}

$$\alpha \propto \alpha_0^\alpha \frac{1}{\sqrt{2\sigma}} \exp\left[-\frac{(E_{\text{G}} - E_{\text{G,mean}})^2}{2\sigma^2}\right] \alpha_0(h\nu, E_{\text{G}}) dE_{\text{G}} \quad (2)$$

Shklovskii and Efros also related α to the mean amplitude of electrostatic potential fluctuations (γ_{EPF}) due to a random distribution of charged defects, namely,⁴¹

$$\alpha \propto \exp\left[-\frac{2}{5\sqrt{\pi}} \left(\frac{E_{\text{G}} - h\nu}{\gamma_{\text{EPF}}/2}\right)^{-5/4}\right] \quad (3)$$

Therefore, the above absorption models can be applied to a plot of $\alpha \propto -\ln[1 - \text{EQE}(h\nu)]$ versus $h\nu$ (Figure 3c). It is apparent that the application of a single absorption model to the data does not adequately describe the observed behavior. In this instance, a combination of BGF and EPF models provides the best data fit. All device types show a similar trend for EPF (23, 23, and 26 meV for devices H, D, and E, respectively). This is in good agreement with the values of the

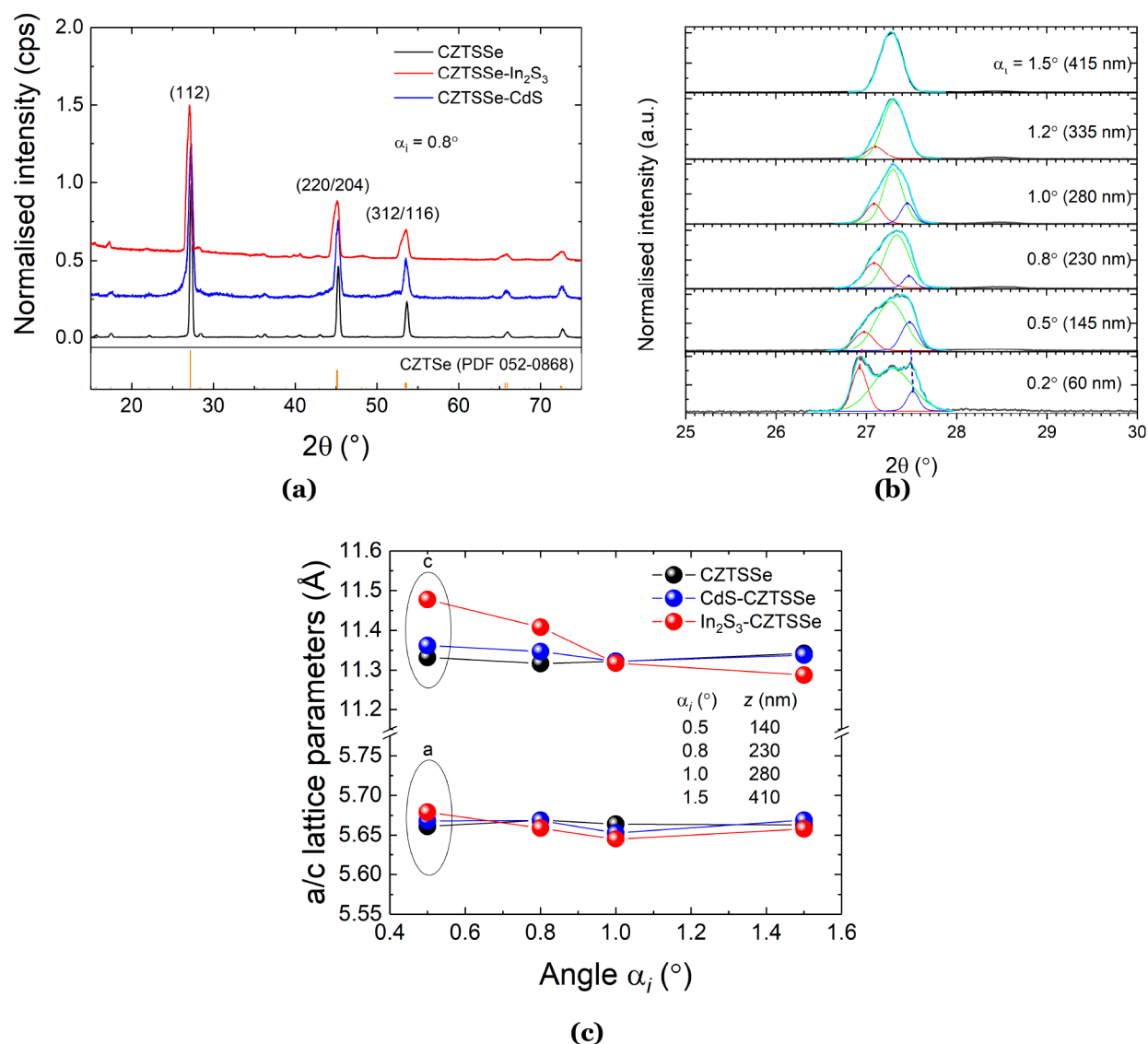


Figure 4. (a) GIXRD patterns of bare CZTSSe, CZTSSe–In₂S₃, and CZTSSe–CdS films on Mo-coated SLG at an incidence angle α_i of 0.5° with peaks referenced to CZTSe (PDF 058-0868). (b) Normalized GIXRD patterns of the (112) peak for the SLG-Mo–CZTSSe–In₂S₃ film stack at a series of incidence angles. The corresponding X-ray penetration depths at different incident angles given in parentheses are calculated based on the attenuation law. (c) *a/c* lattice parameters of the CZTSSe absorbers in the respective film stacks for the range of α_i values between 0.2 and 1.5°.

exponential tail states characterized by the Urbach energy of the CZTSSe absorber in each device (Figure S4). However, there is a considerable difference in the BGF values, with γ_{BGF} as high as 188 meV in device D compared to 146 and 125 meV for devices H and E, respectively. This increase can potentially be associated with a higher degree of In diffusion following two successive heat treatments of the buffer layers during the fabrication of this device structure (see the Methods section). An in-depth study of the material characteristics of the buffer and CZTSSe absorber layers in each device was conducted to elucidate the cause of the differences in performance observed during electrical characterization of the three device types.

DISCUSSION

XRD Analysis. Microstructural analysis was performed by GIXRD on SLG-Mo–CZTSSe, SLG-Mo–CZTSSe–In₂S₃, and SLG-Mo–CZTSSe–CdS film stacks. In the GIXRD patterns, depth profile information was obtained by performing detector scans with fixed incidence angles of 0.5, 0.8, 1.0, and

1.5°. By varying the incidence angle, the penetration depth of X-rays is varied accordingly and can be calculated based on α_i and material properties (see the Supporting Information). Penetration depths for $\alpha_i = 0.5, 0.8, 1.0,$ and 1.5° were calculated according to the method detailed in the Supporting Information and determined to be ca. 140, 230, 280, and 410 nm, respectively.

Figure 4a shows the representative diffractograms of film stacks obtained at an angle of 0.5°. All GIXRD spectra reveal distinct peaks of the (112), (220), and (312) planes, which can be assigned to kesterite CZTSe (PDF 052-0868). The peaks for the SLG-Mo–CZTSSe–In₂S₃ film stack are broad compared to those of the other film stacks. The (112) peaks of the SLG-Mo–CZTSSe–In₂S₃ film stack at a series of incidence angles are therefore normalized and exhibit shoulder peaks, as shown in Figure 4b. When the incidence angle is set at 0.2°, the X-ray penetration depth is calculated to be only ca. 60 nm. This is very close to the actual thickness of the top In₂S₃ layer (~50 nm, as shown in Figure 7b,c) in the film stack.

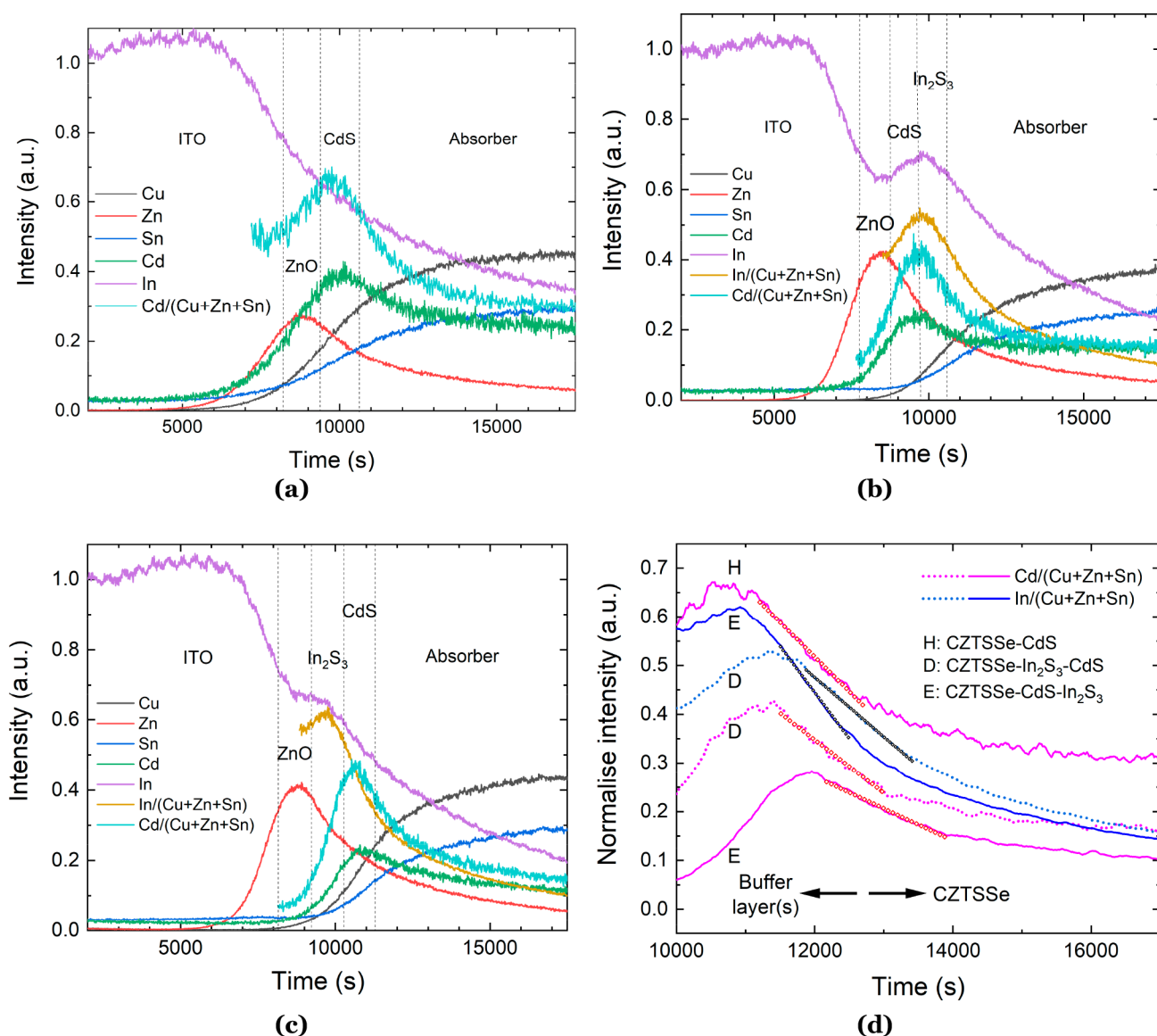


Figure 5. SIMS depth profiles of three solar cells with (a) H: CZTSSe–CdS and (b) D: CZTSSe–In₂S₃–CdS, and (c) E: CZTSSe–CdS–In₂S₃ stacking at the p–n junction, respectively. Both S and Se signals are excluded, and only metallic component elements are included in the figures to reduce the complexity. All data are normalized using the In signal because both samples have ITO layers deposited in the same sample batch. In/metal and Cd/metal ratio curves are used to help to identify different layers, especially the interfaces in solar cells. (d) Slopes of the Cd/metal and In/metal curves in both samples D and E to understand the elemental diffusion at the buffer/absorber interfaces.

The diffraction pattern therefore provides critical information on the crystal structure of materials at the interface between the CZTSSe absorber and In₂S₃ buffer. The diffraction pattern becomes narrow and sharp as the incidence angle increases at the detection region far away from the absorber/buffer interface. Multiplex fits are applied to identify overlapping diffraction peaks of coexistent phases in the broad peak around 27–28°. Apart from the middle main peak belonging to the CZTSSe (112) reflections, there are two shoulder peaks when the incidence angle is shallow. The vertical blue dashed line at a diffraction angle of 27.5° marks the constant position of the β -In₂S₃ (311)^{42,43} diffraction peak at various penetration depths. This indicates that the crystal structure of the In₂S₃ buffer layer is stable and uniform across the thickness of the thin film. When the incidence angle increases to 1.2° or higher, it is hard to observe the In₂S₃ peak anymore because the X-ray detection region is far below the top In₂S₃ thin film and

minimizes the uncertainty from the surface roughness. In addition to the middle CZTSSe (112) reflections, a shoulder peak at a lower diffraction angle indicates increased interplanar lattice separation, likely due to the incorporation of larger In atoms into the CZTSSe crystal lattice at the absorber/buffer interface. The red dashed line indicates continuous evolution of the shoulder peak as the X-ray penetration depth increases away from the interface and less elemental incorporation into the CZTSSe absorber. When the incidence angle increases to 1.5°, no shoulder peak can be observed, indicating that elemental diffusion is constrained in the narrow interface region only. A shoulder on the main (112) CZTSSe peak in the SLG–Mo–CZTSSe–CdS film is also evident at lower incidence angles, which corresponds to the (111) peak in CdS (PDF 01-075-0581; Figure S5). The CdS peak also disappears as the X-ray penetration depth increases. Comple-

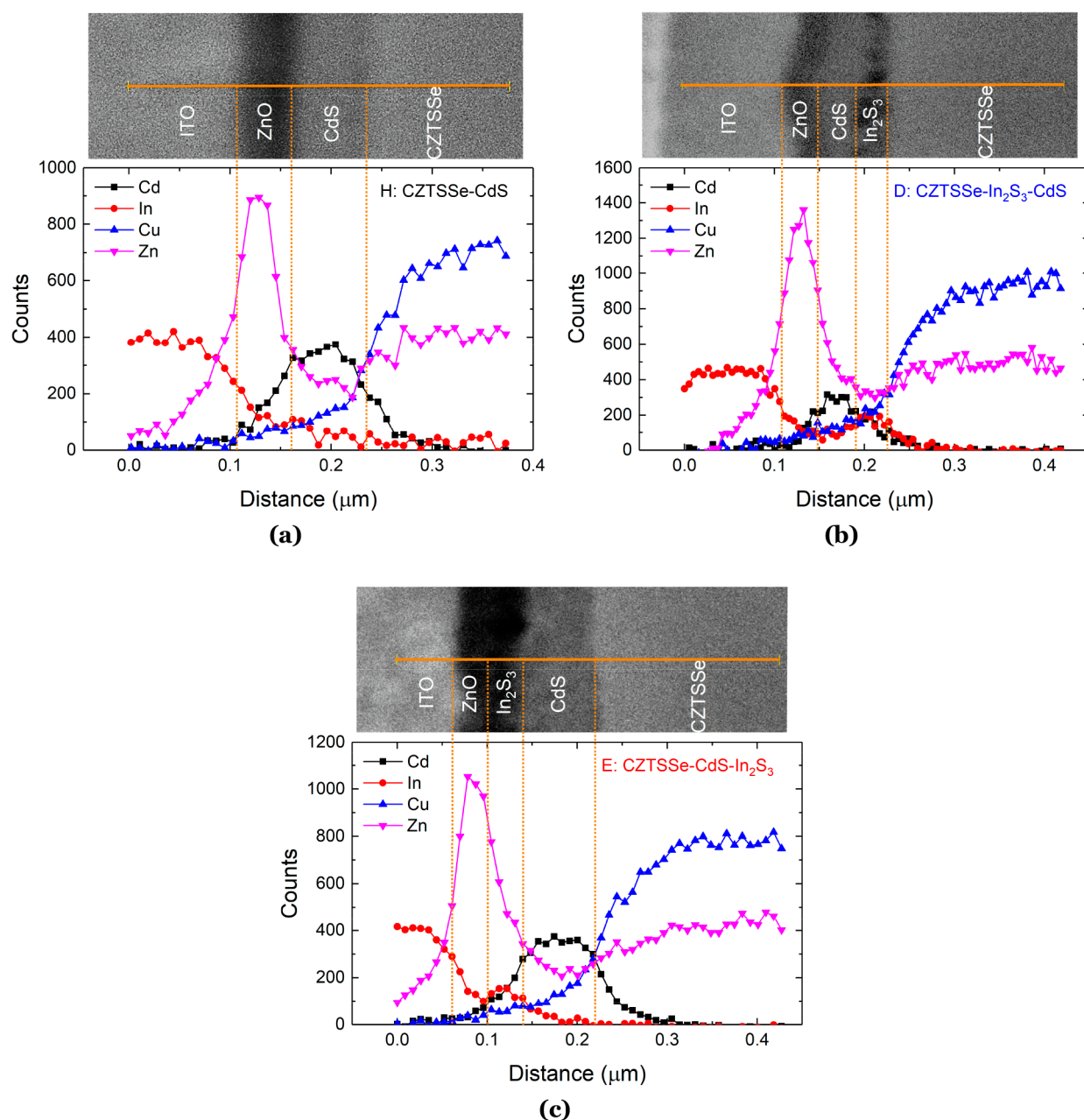


Figure 6. EDX line scans across the buffer/absorber interfaces of devices (a) H: CZTSSe–CdS, (b) D: CZTSSe–In₂S₃–CdS, and (c) E: CZTSSe–CdS–In₂S₃, together with the BSE images of the corresponding FIB device cross sections.

mentary techniques SIMS and EDX were performed to validate this hypothesis.

In addition to the peak broadening, the shifting of the XRD peaks to lower values also implies an increase in the lattice parameter values, which can be further explained by the incorporation of an atom with a larger ionic radius into the CZTSSe crystal lattice. Because all CZTSSe absorbers were fabricated from the same batch of CZTS nanoparticle inks and subject to the same selenization conditions, the shift to lower XRD diffraction angles in the stack with an In₂S₃/CdS buffer infers elemental diffusion from the buffer to the CZTSSe layer. This phenomenon is well documented in kesterite films, where an increasing [Se]/([S] + [Se]) ratio shifts the CZTS 2θ values from 28.44 to 27.16° in CZTSe, given the larger atomic radius of Se (atomic radius ~ 1.98 Å) in comparison to S (atomic radius ~ 1.84 Å).^{13,44–47}

As presented in Figure 4c, the CZTSSe lattice parameters ($a = b \neq c$) for each device type were calculated using the relationships between the Bragg angle 2θ , interplanar spacing d , and lattice parameter a , where $1/d^2 = (h^2 + k^2)/a^2$ and (hkl) is the Miller index of the diffracted plane. There is evidence of changes up to a depth of ~ 230 nm in the lattice structure of the CZTSSe absorber in the film stack with an In₂S₃ buffer layer. The lattice parameters were increased from $a = 5.66$ to 5.68 Å and from $c = 11.33$ to 11.48 Å from the bare CZTSSe absorber to the In₂S₃-buffered absorber. In theory, substitution of the larger In³⁺ ion (ionic radius = 0.80 Å) with the smaller Sn⁴⁺ ion (ionic radius = 0.69 Å) will cause a systematic diffraction angle shift to lower values.^{48–50} Therefore, it is speculated that In diffuses into the CZTSSe region near the In₂S₃/CZTSSe absorber interface following buffer deposition and may induce morphological changes in the CZTSSe

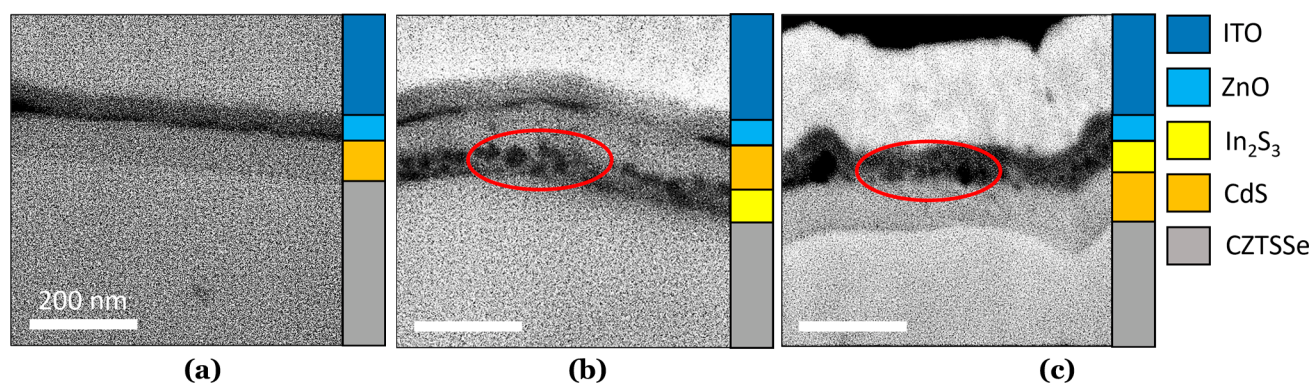


Figure 7. BSE images of device cross sections for (a) H: CZTSSe–CdS, (b) D: CZTSSe–In₂S₃–CdS, and (c) E: CZTSSe–CdS–In₂S₃ solar cells. Heavier elements/films appear as lighter areas in contrast to the images, which enables identification of the individual layers within the structure. The highlighted areas in parts b and c show regions of intermixing of the CdS and In₂S₃ layers.

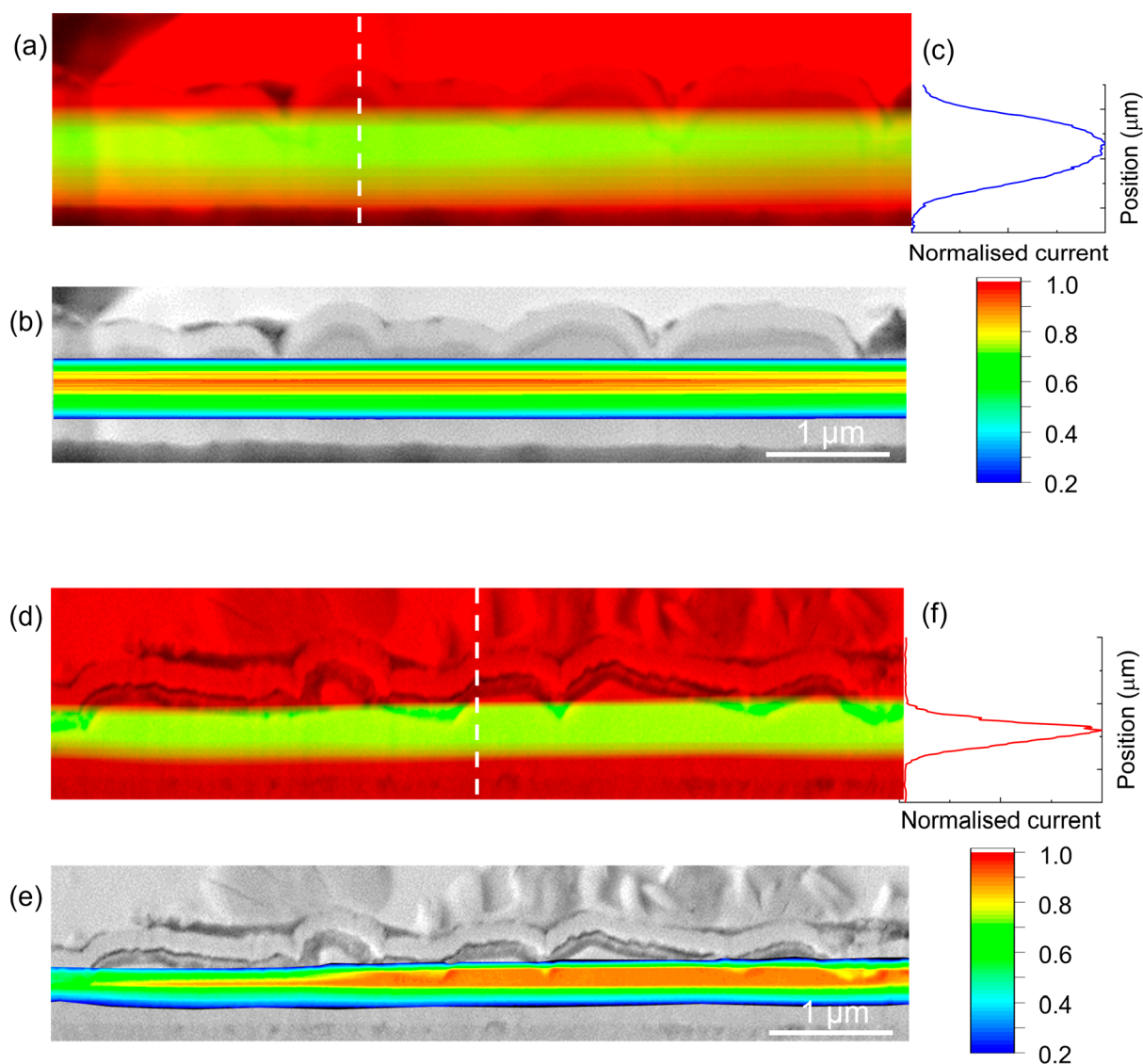


Figure 8. (a and d) SEM cross-sectional images of devices D: CZTSSe–In₂S₃–CdS and E: CZTSSe–CdS–In₂S₃ (red) with a superimposed EBIC signal (green). (b and e) Same SEM cross-sectional images with color maps of the EBIC signals to highlight variations in the signal intensity (signal intensities below 0.2 are not shown to aid visualization). (c and f) Normalized extracted EBIC profiles based on the respective line scans indicated by dashed lines in parts a and d.

absorber near the interface. In the case of the CZTSSe film with a CdS buffer, there is a small increase in the a/c

parameters of the CZTSSe absorber in the near-interface region. This observation again infers the incorporation of an

element with a larger ionic radius into the CZTSSe crystal lattice near the buffer/absorber interface. A previous study found that Cd_{Cu} and/or Cd_{Zn} antisite defects formed up to several hundred nanometers from the heterointerface within the CZTS absorber following a postdeposition heat treatment (PDHT) of the CdS/CZTS film.²

SIMS Analysis. Figure 5 shows the SIMS depth profiles near the absorber/buffer interface for all device structures. In Figure 5b, we can clearly distinguish In_2S_3 and CdS layers with the aid of the Zn signal and In/metal and Cd/metal peaks.

As shown in Figure 5b, the buffer/absorber interface is determined using the peak of the Cd/metal curve. A more detailed discussion of the determination of the buffer/absorber interface is presented in Figure S6. The dashed vertical lines therefore divide the profile into a series of composition zones from the top surface of the solar cell top surface: indium-doped tin oxide (ITO)/ZnO/ In_2S_3 /CdS/CZTSSe absorber. In Figure 5c, however, the Cd and In signals overlap with each other at the p–n junction region. There is only a small shift between the peaks of the Cd and In signals. This indicates that some elemental diffusion might exist at the buffer/absorber interface region. Therefore, the slopes of the In/metal and Cd/metal curves near the buffer/absorber interface are studied in Figure 5d to further understand the elemental diffusion at the p–n junction interface. It can be seen that the slope of the In signal in device type E is sharper (absolute slope = 1.85×10^{-4}) than that of device D (absolute slope = 1.32×10^{-4}). This means that the In signal decays slower in sample D and indicates more In diffused into the bottom CZTSSe absorber.

Electron Microscopy and Composition. EDX mapping and line scans were performed to identify the chemical composition and distribution of the different layers in the region around the buffer/absorber interface (Figure 6). Included in the figures are the corresponding SEM cross sections of the relevant devices obtained by backscattered electron (BSE) imaging. The BSE image contrast depends on the average atomic weight of the elements in the constituent layers; i.e., materials with a higher average atomic weight appear lighter in the BSE images. As such, the individual ITO, ZnO, In_2S_3 , CdS, and CZTSSe layers are clearly distinguishable in all device-type cross sections, and EDX elemental profile data are presented corresponding to the orange line through the cross sections. There is evidence of elemental interdiffusion across the heterojunction of the buffer(s)/CZTSSe films in all device types. Specifically, there is significant diffusion of the metallic element in the buffer (In or Cd) into the absorber when the buffer adjoins the CZTSSe layer. Diffusion of the metallic elements from the buffer to the absorber is promoted by the application of a postdeposition heat treatment following chemical bath deposition (CBD).^{2,19} Researchers at the University of New South Wales found that, following a heterojunction heat treatment (300 °C for 10 min in N_2 atmosphere) of CZTS directly after CBD of CdS, the subsequent CZTS device efficiency improved from ~8% to 11%. The improvement was directly attributed to Cd diffusion into the CZTS absorber up to a depth of ca. 200 nm, forming Cd_{Cu} or Cd_{Zn} antisite defects and Zn diffusion into the CdS layer.

As a result, thin layers of $\text{Cu}_2\text{Cd}_x\text{Zn}_{1-x}\text{SnS}_4$ and $\text{Cd}_x\text{Zn}_{1-x}\text{S}$ formed around the buffer/absorber interface, improving the energy-band alignment at the junction and reducing interface recombination.² Figure 7 shows BSE images of the top window–buffer–absorber layers of the respective CZTSSe

solar cells. In both devices with a dual buffer, there is evidence of intermixing of the layers at the CdS/ In_2S_3 interface. This intermixing of the buffer layers may arise from the successive heat treatments (200 °C in air for 10 min), following deposition of the individual buffers.

Electron-Beam-Induced Current (EBIC). The charge-carrier collection behavior in the devices with a dual buffer was investigated by means of EBIC measurements on flat cross sections obtained by focused-ion-beam (FIB) milling (Figure S7). EBIC measurements visualize the depth-dependent collection of photogenerated carriers in the semiconductor materials in the CZTSSe solar cells. The SEM images (red) are overlaid with the normalized EBIC signal (green), as shown in parts a (device D) and d (device E) of Figure 8. The brightest areas in the EBIC signal show regions of higher current collection over the scanned area of the device cross section and are a measure of the electric field that separates the generated electron–hole (e–h) pairs. The peak of the electric field appears to be broader and generated deeper within the CZTSSe absorber bulk in device D compared to device E. Color maps of the EBIC signals were created to detail the variation in the signal intensity across the device cross sections (Figure 8b,e). For better visualization, EBIC signals below 0.2 are not shown. In the case of device E, a large area of relatively high EBIC signals (red region of the color map) is observed within the CZTSSe absorber close to the CdS/CZTSSe interface, compared to a narrower region of high signal intensity observed in device D (Figure 8b,e). Because the SCR width in device E is ca. 80 nm (determined from C–V measurements), the e–h pairs generated deeper inside the absorber bulk have to diffuse greater distances in order to be effectively separated by the electric field associated with the p–n junction. The higher EBIC signal extending over a larger area in the CZTSSe absorber of device E suggests that the minority carriers (electrons) have a greater minority carrier diffusion length (L_D) than counterpart device D. Approximate L_D values were determined from the absorption coefficient data for the CZTSSe absorbers and the EQE spectra for the respective devices (see the Supporting Information and Figure S8). Subsequent L_D values of ca. 120 and 300 nm for devices D and E were obtained, respectively, which are in good agreement with the observed EBIC signals generated in the device cross sections. Similar results have also been reported for kesterite solar cells.^{51–53} EBIC line profiles perpendicular to the p–n junction were extracted at positions indicated by the dashed white lines on the SEM images and the corresponding normalized integrated EBIC signal ($I_{\text{EBIC, norm}}$) displayed in Figure 8c,f. The EBIC signal in device D presents as a broad signal expanding almost the full width of the CZTSSe absorber, with its peak deep within the bulk.

In contrast, device E has an EBIC line profile with a narrow peak located closer to the buffer/absorber interface. For comparison, EBIC line profiles were plotted in relation to their position from the buffer/CZTSSe interface for both device types (Figure 9). The dashed lines in the figure represent the optimal carrier collection lengths $w_{\text{SCR}} + L_d$ within which the generated e–h pairs from the impinging electron beam can be separated and extracted from the devices. The peak of the electric field in device E lies within this region, leading to improved charge separation and carrier transport and, consequently, a higher J_{SC} .

The opposite effect is true for device D, where peak e–h generation is deeper with the absorber bulk and is susceptible

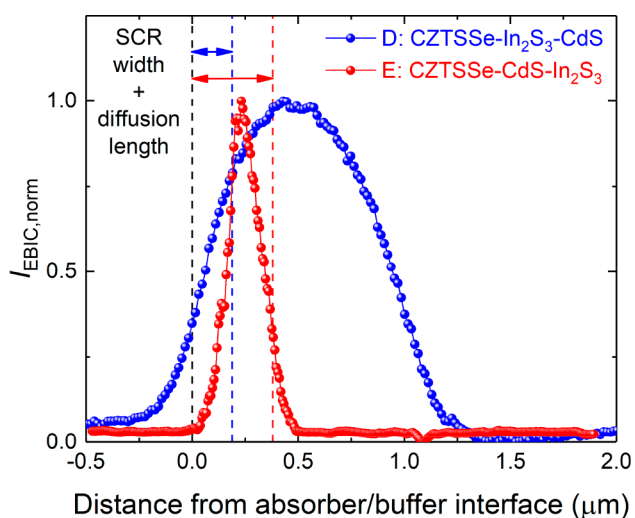


Figure 9. Quantitative EBIC current data as a function of the beam position relative to the devices D: CZTSSe–In₂S₃–CdS and E: CZTSSe–CdS–In₂S₃ extracted from the respective line scans in Figure 8a,d. The dashed red and blue lines represent the sum of the SCR width and minority carrier diffusion length for each device determined from C–V and EQE measurements, respectively.

to higher carrier recombination. This could account, in part, for the lower J_{SC} in these devices compared with E devices. Additionally, the raw EBIC signal observed in D was lower than that in E considering the identical measurement conditions for both types of devices (Figure S9).

CONCLUSION

In summary, CZTSSe solar cells with a combination of CdS and In₂S₃ buffer layers were compared with standard devices with a single CdS layer. Devices with the structure CZTSSe–CdS–In₂S₃ generally performed better than standard devices, with the best device achieving a maximum conversion efficiency of 7.75% (an increase of over 10% compared to the best standard device). Conversely, devices with a CZTSSe–In₂S₃–CdS structure typically demonstrated lower V_{OC} and, as a consequence, had lower overall efficiency compared to standard and CZTSSe–CdS–In₂S₃ devices. CZTSSe–CdS–In₂S₃ devices also showed an appreciable reduction in reverse saturation currents in the SCRs and QNRs of the CZTSSe absorbers. Compositional analysis of the absorber/buffer interfacial region of the CZTSSe solar cells identified significant Cd diffusion from CdS into the CZTSSe absorber in the CZTSSe–CdS–In₂S₃ device and is correlated to the double postdeposition heat treatment of the CdS layer during dual buffer deposition. Cd diffusion has been shown to be beneficial to the device performance by forming a thin layer of Cu₂Cd_xZn_{1-x}(S,Se)₄ on the absorber face, which promotes a more favorable band alignment. Consequently, recombination at the heterojunction region is significantly reduced. The opposite is true for devices with a CZTSSe–In₂S₃–CdS structure. In diffusion into the CZTSSe absorber is also observed as a result of the double heat treatment of the In₂S₃ layer, which serves to increase the p-type doping of the absorber believed to be caused by the formation of acceptor antisite defects In_{Sn}. The width of the SCR is reduced consequently. EBIC measurements revealed that peak e–h generation occurred closer to the p–n (absorber/buffer) junction in the CZTSSe–CdS–In₂S₃ device, which facilitates

charge extraction due to the larger “effective” diffusion length of minority carriers in this device. Conversely, maximum e–h generation takes place deeper into the bulk of the CZTSSe absorber of the CZTSSe–In₂S₃–CdS solar cell, which suffers from a shorter “effective” diffusion length and a higher recombination in the SCR. The device performance is negatively impacted by these factors. This study demonstrates the importance of a quality absorber/buffer interface in achieving efficient solar cells and the positive effects of Cd diffusion on the CZTSSe device performance.

METHODS

CZTS Nanoparticle Inks. CZTS nanoparticles were fabricated using a hot-injection method where a sulfur–oleylamine (OLA) solution was injected into a hot metallic precursors–OLA solution under air-free conditions. The metallic precursor molar ratios were chosen to be Cu/(Zn + Sn) = 0.79 and Zn/Sn = 1.27, achieved by using 1.34 mmol of Cu(acac)₂, 0.95 mmol of Zn(acac)₂, and 0.75 mmol of Sn(acac)₂Cl₂ (where acac = acetylacetonate) as the metallic source to guarantee a Cu-poor, Zn-rich composition region for high solar cell efficiencies. After a reaction at 225 °C for 30 min, the as-synthesized nanoparticles were precipitated and washed twice by using isopropyl alcohol and toluene. The collected CZTS nanoparticles were dispersed with the aid of sonication to provide CZTS nanoparticle inks with a concentration of ~200 mg/mL. More details have been described in our previous works.^{7,13}

Thin-Film Deposition. The resulting nanoparticle inks were deposited on Mo–glass substrates via spin-coating.²⁴ Approximately 30 μL of the concentrated ink was applied onto a square (2.5 cm × 2.5 cm) Mo-coated glass substrate at a speed of 1200 rpm for 5 s. The samples were then dried on a hot plate at 150 °C for 30 s and then at 300 °C in air for 30 s (hereafter “soft-baking”) to remove the residual solvents. The thickness of the deposited thin films could be accurately controlled and reproduced by repeated spin-coating and soft-baking procedures. A thickness of ~1 nm was set for efficient light absorption in all thin films.

Dual Buffer Structure. CBD was used to deposit the buffer layers of CdS and In₂S₃. Specifically, a CdS thin film was fabricated by using cadmium sulfate as the Cd source, thiourea as the S source, and ammonium hydroxide to adjust the pH around 11.9. In terms of In₂S₃ deposition, samples were immersed in a solution composed of indium chloride (10 mM), thioacetamide (0.1 M), and acetic acid (0.1 M) at 70 °C to deposit an In₂S₃ coating on the CZTSSe absorber, with details given in elsewhere.¹⁹ Typical thicknesses of the CdS and In₂S₃ layers are ~70 and ~50 nm, respectively. For the dual buffer device, a bottom buffer layer was deposited first, followed by a top buffer layer to provide a CdS–In₂S₃ or In₂S₃–CdS dual buffer structure. After each buffer layer deposition, the samples were removed from the bath, rinsed with deionized water, dried under a nitrogen stream, and then annealed at 200 °C for different times, i.e., CdS for 10 min and In₂S₃ for 2 min and 10 min in air.

PV Device Fabrication. A solar cell device was completed by the addition of the transparent oxide layers, including *i*-ZnO (~35 nm) and ITO (~200 nm) layers via magnetron sputtering. Ni (~50 nm) and Al (~1 μm) layers were then deposited through a shadow mask by an electron beam to form the front contact grids. Devices were electrically isolated by using mechanical scribing to define a device area of 0.16 mm².

Solar Cell Characterization. Electrical characterization was performed using a Keithley 2400 sourcemeter and Abet Technologies Sun 2000 solar simulator with an air mass 1.5 spectrum set at 100 mW/cm². EQE measurements were performed using a Betham Instruments PVE300 spectral response system with a W light source (calibrated using a Si–InGaAs reference cell). C–V measurements were performed using an Agilent E4980a LCR meter at a frequency of 100 kHz with bias voltages from –0.8 to +0.8 V. Elemental depth profiling was performed by SIMS using a primary Ar⁺ beam of 4 keV, a crater area of 500 × 500 μm², and a gating of 10%. For GIXRD

measurements, a Siemens D-5000 diffractometer using a Cu $K\alpha$ radiation source ($\lambda = 0.154$ nm) was used at a beam voltage of 40 kV and a beam current of 50 mA in the parallel beam setup. In this work, a Tescan Mira 3 field-emission-gun scanning electron microscope was used for SEM imaging, together with an Oxford Instruments X-Max X-ray spectrometer fitted with a 20 mm² detector operating at 10–20 kV for EDX measurements.

EBIC Measurement. Samples were prepared for EBIC analysis using FIB cross-section milling with a Ga liquid metal ion source FEI Helios Nano Lab 600 dual-beam system. A series of in situ polishing steps were performed to produce a clean surface with minimal beam damage. Simultaneous EBIC analysis and secondary electron imaging were carried out with a Hitachi SU-70 microscope, with EBIC signals being collected through a Matelect ISM6 specimen current amplifier, using a beam voltage of 5 kV and a current of 0.75 nA. The image filter frequency was set to 10 kHz; this eliminated both noise and fine image detail, and so the images in this paper show the average position of the junctions in the PV devices.

■ ASSOCIATED CONTENT

SI Supporting Information

The Supporting Information is available free of charge at <https://pubs.acs.org/doi/10.1021/acsaem.3c01622>.

Double-diode fit to a raw J - V curve of an example CZTSSe H reference device, built-in voltage V_{bi} for all CZTSSe device types, CZTSSe absorber band-gap E_G determination from the EQ spectra for all CZTSSe device types, X-ray penetration depth method and calculation, alignment of the SIMS profiles using the Zn peak for all CZTSSe samples, SEM FIB cross sections for dual buffer CZTSSe devices, minority carrier diffusion length calculation from the EQE spectra for all CZTSSe devices, and raw EBIC line scan data for dual buffer CZTSSe devices (PDF) (ZIP)

■ AUTHOR INFORMATION

Corresponding Author

Yongtao Qu – Department of Mathematics, Physics and Electrical Engineering, Northumbria University, Newcastle-upon-Tyne NE1 8ST, United Kingdom; Email: y.qu@northumbria.ac.uk

Authors

Stephen Campbell – Department of Mathematics, Physics and Electrical Engineering, Northumbria University, Newcastle-upon-Tyne NE1 8ST, United Kingdom; orcid.org/0000-0002-4340-4086

Guillaume Zoppi – Department of Mathematics, Physics and Electrical Engineering, Northumbria University, Newcastle-upon-Tyne NE1 8ST, United Kingdom; orcid.org/0000-0003-3622-6899

Leon Bowen – Department of Physics, Durham University, Durham DH1 3LE, United Kingdom

Pietro Maiello – Department of Mathematics, Physics and Electrical Engineering, Northumbria University, Newcastle-upon-Tyne NE1 8ST, United Kingdom

Vincent Barrioz – Department of Mathematics, Physics and Electrical Engineering, Northumbria University, Newcastle-upon-Tyne NE1 8ST, United Kingdom

Neil S. Beattie – Department of Mathematics, Physics and Electrical Engineering, Northumbria University, Newcastle-upon-Tyne NE1 8ST, United Kingdom; orcid.org/0000-0002-0098-4420

Complete contact information is available at: <https://pubs.acs.org/doi/10.1021/acsaem.3c01622>

Notes

The authors declare no competing financial interest.

■ ACKNOWLEDGMENTS

The authors appreciate the support from British Council Newton Fund Institutional Links Grant (UK-Turkey) in Ultralight Absorber for Remote Energy Source (No. 623804307). The authors also acknowledge the Engineering and Physical Sciences Research Council for funding through The North East Centre for Energy Materials (EP/R021503/1) and Reimagining Photovoltaics Manufacturing (EP/W010062/1).

■ REFERENCES

- (1) <http://www.shell.com/skyscenario>.
- (2) Yan, C.; Huang, J.; Sun, K.; Johnston, S.; Zhang, Y.; Sun, H.; Pu, A.; He, M.; Liu, F.; Eder, K.; Yang, L.; Cairney, J. M.; Ekins-Daukes, N. J.; Hameiri, Z.; Stride, J. A.; Chen, S.; Green, M. A.; Hao, X. $\text{Cu}_2\text{ZnSnS}_4$ solar cells with over 10% power conversion efficiency enabled by heterojunction heat treatment. *Nat. Energy* **2018**, *3*, 764–772.
- (3) Li, J.; Huang, J.; Ma, F.; Sun, H.; Cong, J.; Privat, K.; Webster, R. F.; Cheong, S.; Yao, Y.; Chin, R. L.; Yuan, X.; He, M.; Sun, K.; Li, H.; Mai, Y.; Hameiri, Z.; Ekins-Daukes, N. J.; Tilley, R. D.; Unold, T.; Green, M. A.; Hao, X. Unveiling microscopic carrier loss mechanisms in 12% efficient $\text{Cu}_2\text{ZnSnSe}_4$ solar cells. *Nat. Energy* **2022**, *7*, 754–764.
- (4) Zhou, J.; Xu, X.; Wu, H.; Wang, J.; Lou, L.; Yin, K.; Gong, Y.; Shi, J.; Luo, Y.; Li, D.; Xin, H.; Meng, Q. Control of the phase evolution of kesterite by tuning of the selenium partial pressure for solar cells with 13.8% certified efficiency. *Nat. Energy* **2023**, *8*, 526.
- (5) Green, M. A.; Dunlop, E. D.; Yoshita, M.; Kopidakis, N.; Bothe, K.; Siefert, G.; Hao, X. Solar cell efficiency tables (version 62). *Prog. Photovoltaics* **2023**, *31*, 651.
- (6) NREL, Best Research-Cell Efficiency Chart. <https://www.nrel.gov/pv/cell-efficiency.html>, 2023.
- (7) Qu, Y.; Zoppi, G.; Beattie, N. S. Selenization Kinetics in $\text{Cu}_2\text{ZnSn}(\text{S},\text{Se})_4$ solar cells prepared from nanoparticle inks. *Sol. Energy Mater. Sol. Cells* **2016**, *158*, 130–137.
- (8) Qu, Y.; Zoppi, G.; Beattie, N. S. The role of nanoparticle inks in determining the performance of solution processed $\text{Cu}_2\text{ZnSn}(\text{S},\text{Se})_4$ thin film solar cells. *Progress in Photovoltaics: Research and Applications* **2016**, *24*, 836–845.
- (9) Qu, Y.; Zoppi, G.; Miles, R. W.; Beattie, N. S. Influence of reaction conditions on the properties of solution-processed $\text{Cu}_2\text{ZnSnS}_4$ nanocrystals. *Materials Research Express* **2014**, *1*, 045040.
- (10) Xu, X.; Qu, Y.; Barrioz, V.; Zoppi, G.; Beattie, N. S. Reducing series resistance in $\text{Cu}_2\text{ZnSn}(\text{S},\text{Se})_4$ nanoparticle ink solar cells on flexible molybdenum foil substrates. *RSC Adv.* **2018**, *8*, 3470–3476.
- (11) Antunez, P. D.; Bishop, D. M.; Luo, Y.; Haight, R. Efficient kesterite solar cells with high open-circuit voltage for applications in powering distributed devices. *Nature Energy* **2017**, *2*, 884–890.
- (12) Fonoll-Rubio, R.; Andrade-Arvizu, J.; Blanco-Portals, J.; Becerril-Romero, I.; Guc, M.; Saucedo, E.; Peñó, F.; Calvo-Barrio, L.; Ritzer, M.; Schnohr, C. S.; Placidi, M.; Estradé, S.; Izquierdo-Roca, V.; Pérez-Rodríguez, A. Insights into interface and bulk defects in a high efficiency kesterite-based device. *Energy Environ. Sci.* **2021**, *14*, 507–523.
- (13) Qu, Y.; Chee, S. W.; Duchamp, M.; Campbell, S.; Zoppi, G.; Barrioz, V.; Giret, Y.; Penfold, T. J.; Chaturvedi, A.; Mirsaidov, U.; Beattie, N. S. Real-time electron nanoscopy of photovoltaic absorber formation from kesterite nanoparticles. *ACS Applied Energy Materials* **2020**, *3*, 122–128.

- (14) Yan, C.; Liu, F.; Sun, K.; Song, N.; Stride, J. A.; Zhou, F.; Hao, X.; Green, M. Boosting the efficiency of pure sulfide CZTS solar cells using the In/CD-based hybrid buffers. *Sol. Energy Mater. Sol. Cells* **2016**, *144*, 700–706.
- (15) Jiang, F.; Ozaki, C.; Gunawan, Harada, T.; Tang, Z.; Minemoto, T.; Nose, Y.; Ikeda, S. Effect of indium doping on surface optoelectrical properties of $\text{Cu}_2\text{ZnSnS}_4$ photoabsorber and interfacial/photovoltaic performance of cadmium free $\text{In}_2\text{S}_3/\text{Cu}_2\text{ZnSnS}_4$ heterojunction thin film solar cell. *Chem. Mater.* **2016**, *28*, 3283–3291.
- (16) Barkhouse, D. A.; Haight, R.; Sakai, N.; Hiroi, H.; Sugimoto, H.; Mitzi, D. B. CD-free buffer layer materials on $\text{Cu}_2\text{ZnSn}(\text{S}_x\text{Se}_{1-x})_4$: Band alignments with ZnO , ZnS , and In_2S_3 . *Appl. Phys. Lett.* **2012**, *100*, 193904.
- (17) Campbell, S.; Qu, Y.; Gibbon, J.; Edwards, H. J.; Dhanak, V. R.; Tiwari, D.; Barrioz, V.; Beattie, N. S.; Zoppi, G. Defect limitations in $\text{Cu}_2\text{ZnSn}(\text{S},\text{Se})_4$ solar cells utilizing an In_2S_3 buffer layer. *J. Appl. Phys.* **2020**, *127*, 205305.
- (18) Kim, J.; Hiroi, H.; Todorov, T. K.; Gunawan, O.; Kuwahara, M.; Gokmen, T.; Nair, D.; Hopstaken, M.; Shin, B.; Lee, Y. S.; Wang, W.; Sugimoto, H.; Mitzi, D. B. High efficiency $\text{Cu}_2\text{ZnSn}(\text{S},\text{Se})_4$ solar cells by applying a double $\text{In}_2\text{S}_3/\text{CdS}$ emitter. *Adv. Mater.* **2014**, *26*, 7427–7431.
- (19) Campbell, S.; Duchamp, M.; Ford, B.; Jones, M.; Nguyen, L. L.; Naylor, M. C.; Xu, X.; Maiello, P.; Zoppi, G.; Barrioz, V.; Beattie, N. S.; Qu, Y. Recovery mechanisms in aged kesterite solar cells. *ACS Applied Energy Materials* **2022**, *5*, 5404–5414.
- (20) Cantas, A.; Turkoglu, F.; Meric, E.; Akca, F. G.; Ozdemir, M.; Tarhan, E.; Ozyuzer, L.; Aygun, G. Importance of CdS buffer layer thickness on $\text{Cu}_2\text{ZnSnS}_4$ -based solar cell efficiency. *J. Phys. D: Appl. Phys.* **2018**, *51*, 275501.
- (21) Wang, W.; Winkler, M. T.; Gunawan, O.; Gokmen, T.; Todorov, T. K.; Zhu, Y.; Mitzi, D. B. Device characteristics of CZTSSe thin-film solar cells with 12.6% efficiency. *Adv. Energy Mater.* **2014**, *4*, 1301465.
- (22) Shin, B.; Zhu, Y.; Bojarczuk, N. A.; Jay Chey, S.; Guha, S. Control of an interfacial MoSe₂ Layer in $\text{Cu}_2\text{ZnSnSe}_4$ thin film solar cells: 8.9% power conversion efficiency with a TiN diffusion barrier. *Appl. Phys. Lett.* **2012**, *101*, 053903.
- (23) Scragg, J. J.; Kubart, T.; Wätjen, J. T.; Ericson, T.; Linnarsson, M. K.; Platzer-Björkman, C. Effects of back contact instability on $\text{Cu}_2\text{ZnSnS}_4$ devices and processes. *Chem. Mater.* **2013**, *25*, 3162–3171.
- (24) Campbell, S.; Qu, Y.; Bowen, L.; Chapon, P.; Barrioz, V.; Beattie, N.; Zoppi, G. Influence of OLA and FA ligands on the optical and electronic properties of $\text{Cu}_2\text{ZnSn}(\text{S},\text{Se})_4$ thin films and solar cells prepared from nanoparticle inks. *Sol. Energy* **2018**, *175*, 101–109.
- (25) Chen, S.; Walsh, A.; Gong, X.-G.; Wei, S.-H. Classification of lattice defects in the Kesterite $\text{Cu}_2\text{ZnSnS}_4$ and $\text{Cu}_2\text{ZnSnSe}_4$ earth-abundant solar cell absorbers. *Adv. Mater.* **2013**, *25*, 1522–1539.
- (26) Barkhouse, D. A.; Gunawan, O.; Gokmen, T.; Todorov, T. K.; Mitzi, D. B. Device characteristics of a 10.1% hydrazine-processed $\text{Cu}_2\text{ZnSn}(\text{S},\text{Se})_4$ solar cell. *Progress in Photovoltaics: Research and Applications* **2012**, *20*, 6–11.
- (27) Duan, H.-S.; Yang, W.; Bob, B.; Hsu, C.-J.; Lei, B.; Yang, Y. The role of sulfur in solution-processed $\text{Cu}_2\text{ZnSn}(\text{S},\text{Se})_4$ and its effect on defect properties. *Advanced Functional Materials* **2013**, *23*, 1466–1471.
- (28) Werner, F.; Babbe, F.; Elanzeery, H.; Siebentritt, S. Can we see defects in capacitance measurements of thin-film solar cells? *Progress in Photovoltaics: Research and Applications* **2019**, *27*, 1045–1058.
- (29) Werner, F.; Babbe, F.; Burkhart, J.; Spindler, C.; Elanzeery, H.; Siebentritt, S. Inter-diffusion and doping gradients at the buffer/absorber interface in thin-film solar cells. *ACS Appl. Mater. Interfaces* **2018**, *10*, 28553–28565.
- (30) Andres, C.; Schwarz, T.; Haass, S.; Weiss, T.; Carron, R.; Caballero, R.; Figi, R.; Schreiner, C.; Bürki, M.; Tiwari, A.; Romanyuk, Y. E. Decoupling of optoelectronic properties from morphological changes in sodium treated kesterite thin film solar cells. *Sol. Energy* **2018**, *175*, 94–100.
- (31) Xu, X.; Qu, Y.; Campbell, S.; Le Garrec, M.; Ford, B.; Barrioz, V.; Zoppi, G.; Beattie, N. S. Solution processing route to Na incorporation in CZTSSe nanoparticle ink solar cells on foil substrate. *Journal of Materials Science: Materials in Electronics* **2019**, *30*, 7883–7889.
- (32) Heath, J.; Zabierowski, P. Capacitance spectroscopy of thin-film solar cells. *Advanced Characterization Techniques for Thin Film Solar Cells* **2011**, 81–105.
- (33) Khadka, D. B.; Kim, S.; Kim, J. A nonvacuum approach for fabrication of $\text{Cu}_2\text{ZnSnSe}_4/\text{In}_2\text{S}_3$ thin film solar cell and optoelectronic characterization. *J. Phys. Chem. C* **2015**, *119*, 12226–12235.
- (34) Pei, Y.; Guo, J.; Kou, D.; Zhou, W.; Zhou, Z.; Tian, Q.; Meng, Y.; Wu, S. Precise-tuning the In content to achieve high fill factor in hybrid buffer structured $\text{Cu}_2\text{ZnSn}(\text{S},\text{Se})_4$ solar cells. *Sol. Energy* **2017**, *148*, 157–163.
- (35) Liu, F.; Yan, C.; Sun, K.; Zhou, F.; Hao, X.; Green, M. A. Light-bias-dependent external quantum efficiency of Kesterite $\text{Cu}_2\text{ZnSnS}_4$ solar cells. *ACS Photonics* **2017**, *4*, 1684–1690.
- (36) Xiao, Z.; Luan, H.; Liu, R.; Yao, B.; Li, Y.; Ding, Z.; Yang, G.; Deng, R.; Wang, G.; Zhang, Z.; Zhang, L.; Zhao, H. Behavior of indium alloying with $\text{Cu}_2\text{ZnSn}(\text{S},\text{Se})_4$ and its effect on performances of $\text{Cu}_2\text{ZnSn}(\text{S},\text{Se})_4$ -based solar cell. *J. Alloys Compd.* **2018**, *767*, 439–447.
- (37) Campbell, S.; Qu, Y.; Major, J. D.; Lagarde, D.; Labbé, C.; Maiello, P.; Barrioz, V.; Beattie, N. S.; Zoppi, G. Direct evidence of causality between chemical purity and band-edge potential fluctuations in nanoparticle ink-based $\text{Cu}_2\text{ZnSn}(\text{S},\text{Se})_4$ solar cells. *J. Phys. D: Appl. Phys.* **2019**, *52*, 135102.
- (38) Liu, X. X.; Sites, J. R. Solar-cell collection efficiency and its variation with voltage. *J. Appl. Phys.* **1994**, *75*, 577–581.
- (39) Gokmen, T.; Gunawan, O.; Todorov, T. K.; Mitzi, D. B. Band tailing and efficiency limitation in Kesterite Solar Cells. *Appl. Phys. Lett.* **2013**, *103*. DOI: 10.1063/1.4820250
- (40) Mattheis, J.; Rau, U.; Werner, J. H. Light absorption and emission in semiconductors with band gap fluctuations—a study on $\text{Cu}(\text{In,Ga})\text{Se}_2$ thin films. *J. Appl. Phys.* **2007**, *101*, 113519.
- (41) Shklovskii, B. I.; Efros, A. L. *Electronic properties of doped semiconductors*; Springer Series in Solid-State Sciences; Springer, 1984.
- (42) Yahmadi, B.; Kamoun, N.; Bennaceur, R.; Mnari, M.; Dachraoui, M.; Abdelkrim, K. Structural analysis of indium sulphide thin films elaborated by Chemical Bath Deposition. *Thin Solid Films* **2005**, *473*, 201–207.
- (43) Gao, Z.; Liu, J.; Wang, H. Investigation on growth of In_2S_3 thin films by chemical bath deposition. *Materials Science in Semiconductor Processing* **2012**, *15*, 187–193.
- (44) Ananthoju, B.; Mohapatra, J.; Jangid, M. K.; Bahadur, D.; Medhekar, N. V.; Aslam, M. Cation/anion substitution in $\text{Cu}_2\text{ZnSnS}_4$ for improved photovoltaic performance. *Sci. Rep.* **2016**, *6*. DOI: 10.1038/srep35369
- (45) Singh, A. K.; Aggarwal, G.; Singh, R. K.; Klein, T. R.; Das, C.; Neergat, M.; Kavaipatti, B.; van Hest, M. F. Synthesis of CZTS/Se and their solid solution from electrodeposited Cu-Sn-Zn Metal Precursor: A study of S and Se replacement reaction. *ACS Applied Energy Materials* **2018**, *1*, 3351–3358.
- (46) Riha, S. C.; Parkinson, B. A.; Prieto, A. L. Compositionally tunable $\text{Cu}_2\text{ZnSn}(\text{S}_{1-x}\text{Se}_x)$ nanocrystals: Probing the effect of Se-inclusion in mixed chalcogenide thin films. *Journal of the American Chemical Society* **2011**, *133*, 15272–15275.
- (47) Salomé, P.; Malaquias, J.; Fernandes, P.; Ferreira, M.; da Cunha, A.; Leitao, J.; Gonzalez, J.; Matinaga, F. Growth and characterization of $\text{Cu}_2\text{ZnSn}(\text{S},\text{Se})_4$ thin films for solar cells. *Sol. Energy Mater. Sol. Cells* **2012**, *101*, 147–153.
- (48) Kuo, D.-H.; Tsega, M. Electrical conduction and mobility enhancement in P-type In-doped $\text{Cu}_2\text{ZnSnS}_4$ bulks. *Jpn. J. Appl. Phys.* **2014**, *53*, 035801.
- (49) Li, J.; Wang, H.; Luo, M.; Tang, J.; Chen, C.; Liu, W.; Liu, F.; Sun, Y.; Han, J.; Zhang, Y. 10% efficiency $\text{Cu}_2\text{ZnSn}(\text{S},\text{Se})_4$ thin film

solar cells fabricated by magnetron sputtering with enlarged depletion region width. *Sol. Energy Mater. Sol. Cells* **2016**, *149*, 242–249.

(50) Rajeshmon, V.; Poornima, N.; Sudha Kartha, C.; Vijayakumar, K. Modification of the optoelectronic properties of sprayed In_2S_3 thin films by indium diffusion for application as buffer layer in CZTS based solar cell. *J. Alloys Compd.* **2013**, *553*, 239–244.

(51) Ren, Y.; Richter, M.; Keller, J.; Redinger, A.; Unold, T.; Donzel-Gargand, O.; Scragg, J. J.; Platzer Bjorkman, C. Investigation of the $\text{SnS}/\text{Cu}_2\text{ZnSnS}_4$ interfaces in kesterite thin-film solar cells. *ACS Energy Lett.* **2017**, *2*, 976–981.

(52) Just, J.; Nichterwitz, M.; Lützenkirchen-Hecht, D.; Frahm, R.; Unold, T. Compositional dependence of charge carrier transport in kesterite $\text{Cu}_2\text{ZnSnS}_4$ solar cells. *J. Appl. Phys.* **2016**, *120*, 225703.

(53) Pu, A.; Ma, F.; Yan, C.; Huang, J.; Sun, K.; Green, M.; Hao, X. Sentaurus modelling of 6.9% $\text{Cu}_2\text{ZnSnS}_4$ device based on comprehensive electrical & optical characterization. *Sol. Energy Mater. Sol. Cells* **2017**, *160*, 372–381.